Modelling of the WITT wave energy converter

S. Crowley[a], R. Porter[a,*], D.J. Taunton[b], P.A. Wilson[b]

[a]*School of Mathematics, University of Bristol, University Walk, Bristol, BS8 1TW, UK.*
[b]*Faculty of Engineering and the Environment, University of Southampton, Lanchester Building, Southampton, SO17 1BJ, UK.*

Abstract

The paper describes the theoretical modelling and experimental validation of a novel design of ocean wave energy converter which is comprised of a floating, moored, spherical hull containing a mechanical pendulum arrangement from which power is taken when excited by incident waves. Experimental results are shown to compare favourably with those predicted by the theory. An explicit expression is derived for the capture width of the proposed device in terms of physical and hydrodynamic parameters. This exposes the multiple resonant characteristics of the device which enable it to operate effectively over a broad range of wave periods. The subsequent efficient computations allows a numerical optimisation of the design to be performed over a large space of device parameters and model sea spectrum. The work is focussed towards producing reliable estimates for the power capacity of different sized devices deployed at the EMEC site in Scotland. Predictions compare favourably with existing wave energy converter concepts.

Keywords: wave energy converter, floating sphere, internal pendulum, coupled resonances

1. Introduction

The WITT (Whatever Input to Torque Transfer; see `http://www.witt-energy.com/`; Fig. 1) is a proprietary mechanical device for converting kinetic energy into electrical energy. It is comprised of a heavy compound pendulum connected through a gearbox so that its rotary motion about either of two perpendicular horizontal axes is transferred to a single unidirectional output through a primary axis from which the energy of motion can subsequently be harvested. The WITT is currently being considered for use in a range of small to large scale applications.

The authors on this paper have been involved as part of a wider project to investigate the feasibility of using a WITT housed within a sealed hull to harness the motions induced by ocean waves and convert them into electrical energy. The present paper details a theoretical model which has been developed to describe the operation of a WITT Wave Energy Converter (WITT WEC) and experiments performed to validate its predictions.

The concept of using a mechanical device with heavy counterweights operating inside a sealed hull to absorb wave energy is not new; for example the SEAREV [see 5] and the [18] Penguin. The principle underpinning the successful capture of ocean wave energy lies in amplifying and

*Corresponding authors
Email address: `richard.porter@bristol.ac.uk` (R. Porter)

converting the energy in low frequency, low amplitude waves. The Wello Penguin device appears to do this using the instability of a hull to pitching and rolling motions of a large weight mounted on a vertical axis. In contrast, SEAREV uses the more conventional approach in WEC design of exploiting resonance of the hull and an internal pendulum rotating about a horizontal axis. It is this latter approach which also underpins the current design analysis of the WITT WEC and one which allows us to use existing methodology based on linearised (or small amplitude) theory to predict power capture and device motions across an irregular sea sate. It is the primary purpose of this paper to demonstrate how this is done and to provide initial estimates as to the potential power output from a WITT WEC.

There are several ways in which the WITT WEC design varies from the SEAREV design. Both are designed to operate in the surface of the ocean, but the ability of the pendulum in the WITT to operate about both horizontal axes allows it to extract power from from all wave headings. Moreover, the design of the WITT WEC integrates the sealed hull with a heavy chain catenary mooring system which is crucial in providing device resonances. In contrast, the SEAREV mooring is not an active design component. Thus, we will show later the WITT WEC can exhibit resonance at three distinct periods and this consequently gives the WITT WEC a broadbanded response to incident waves. In contrast the SEAREV [4, Fig. 4], [5, Fig. 12] possesses just two device resonances. There are other differences, perhaps the key one being that the WITT is able to rotate fully through 360 degrees about either axis which means its motion is not mechanically limited, a common problem in converter design.

The theoretical development of the WITT WEC design uses a number of assumptions and approximations which are outlined through the paper. Many of these are based on the use of first order, or small amplitude, theory. These assumptions are made in the hydrodynamic theory describing the manner in which waves interact with the sphere, requiring wave steepness and device motions to be sufficiently small. They are also made in the theoretical model of a catenary mooring system whose first order approximation results in a Hooke's law relation. Moreover, pendulum motions are also assumed to be small to allow linearisation of the underlying mechanical equations. Finally, we assume a simple linear power take-off (PTO) system. In addition, various simplifying model assumptions are made throughout justified as having captured the most important effects. These include, for example, constraining the pendulum to move about only one of its two axes on the assumption that a deployed device would be aligned to operate in a marine environment with a well-understood directional sea state.

The effect of these assumptions are tested by comparing device RAOs to a series of experiments, described later in the paper, which again focus on the main operational elements of the model rather than a fully developed scale model of the WITT WEC.

The theoretical work is most closely related to recent work by two of the current authors on a theoretical WEC design based on a similar principle. Thus [6] considered a long submerged cylinder containing a heavy pendulum allowed to rotate around a single axis and which was tethered to the sea bed and whose cylindrical hull operated as an inverted pendulum using an assumed buoyancy acting to provide a restoring force. That work demonstrated that multiple resonances could be achieved and an optimisation over physically realisable parameters allowed the proposed device to operate close to a theoretical maximum over a broad range of wave periods (roughly 5-11s). The design of [6] is quite different to the WITT WEC the former device principly acting as an attenuator and the latter as a point absorber. However, the concept of using a counterweight is common to both and mathematical ideas developed in [6] can be extended to the moored floating hull design of the WITT WEC. The mathematics here is more complicated with four degrees of freedom here

Figure 1: A photo of a prototype of the WITT pendulum and gearbox mechanism

(hull pitch, heave, surge and pendulum pitch) replacing the two (device surge and pendulum pitch) in [6]. Nevertheless, it is shown that explicit expressions for capture width (a standard measure of power absorption capacity) can be attained in terms of physical and hydrodynamic coefficients. This allows us to theoretically identify aspects of the design which are useful in describing the device operation. Moreover, the computational efficiency offered by the theoretical results used allows us to numerically optimise over physical design parameters and over a realistic wave energy spectra.

Related work on the use of moored spheres as a wave power absorber include [16] who considered a sphere held submerged below the surface with the PTO incorporated into a mooring system. Also, [7] made a theoretical assessment of the impact on power absorption of placing motion constraints on the operation of WECs including a semi-submerged spherical WEC. That study showed, for example, that a surging sphere whose motion is limited to a wave amplitude cannot extract more than 70% of the power incident on the sphere. This rises to 108% when surge motion is limited to two wave amplitudes.

The layout of the paper is as follows. In Section 2, we describe the proposed operation of the WITT WEC and define some of the parameters adopted in the modelling. In Section 3, an outline of the mathematical model is presented focussing on the mechanics and the derivation of expressions useful for calculating the power. The derivation of the equations of motion, the modelling of the mooring system coefficients and the description of a model sea state are relegated to Appendices but will be useful to researchers wanting to follow in detail the modelling and its assumptions. Section 4 describes the modelling used in the wave tank tests and compares experimental results with those predicted by the model. In Section 5 we use the model to predict results for an optimised full scale device and finally in the Conclusions summarise the paper and discuss the proposed design in a wider context of WEC design (see [1]) and describe the direction in which further work will be pursued.

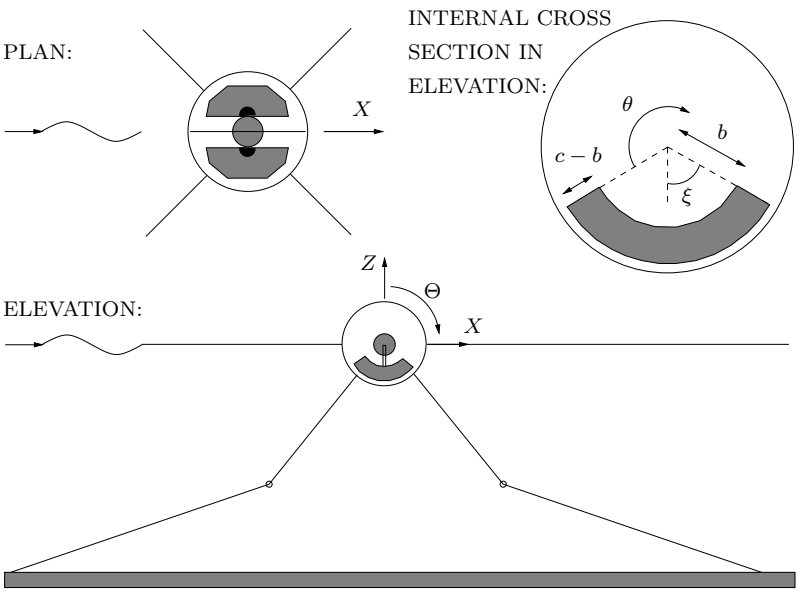

Figure 2: Sketch in plan, elevation and internal cross section (in elevation) of the system, showing directions of modes of motion and definition of the pendulum geometry.

2. Device description

This paper addresses the modelling of a specific embodiment of the proposed WITT WEC in which a WITT device is placed within a semi-immersed sealed spherical hull, which is able to move in heave, surge, and pitch but is restrained by a four-point catenary mooring system in which splayed heavy chains connect the hull of the WEC to the sea floor. This mooring system has the obvious practical role of preventing the WITT WEC from drifting away from its installation site, but it also supplies spring restoring forces to the device when it moves in response to waves. A realistic mooring would include clump weights along an extended section of the mooring line resting on the sea bed which would provide a stiffening of the restoring force for larger device motions anticipated under heavier seas. In our model, we use point masses placed on inextensible light lines to represent the effect of a heavy catenary chain (see Fig. 2).

Internal to the sphere the WITT pendulum which is designed to rotate about both horizontal axis by any amount (see Fig. 1). We model it as a compound pendulum which is vertically axisymmetric formed by an annular sector in cross section. The gearbox within the WITT device selects the input possessing the greatest angular velocity from the two axes to drive the output rather than combining them additively. In practice, this means that a WITT with its primary axis aligned with a principal direction of incoming waves will operate predominately in a single degree of freedom (which we refer to as pendulum pitch) and will only extract energy from pendulum roll motion for wave headings beyond 45° or in the possible event of the onset of parametric instabilities. Therefore, in this model, the pendulum is allowed to rotate in pitch about just one central horizontal axis of the sphere aligned with the crests of the predominant incoming waves (see Fig. 2). Power is assumed to be extracted from a linear damper which acts in proportion to the relative angular velocity of the pendulum with respect to that of the sphere. In our model, two point masses are positioned

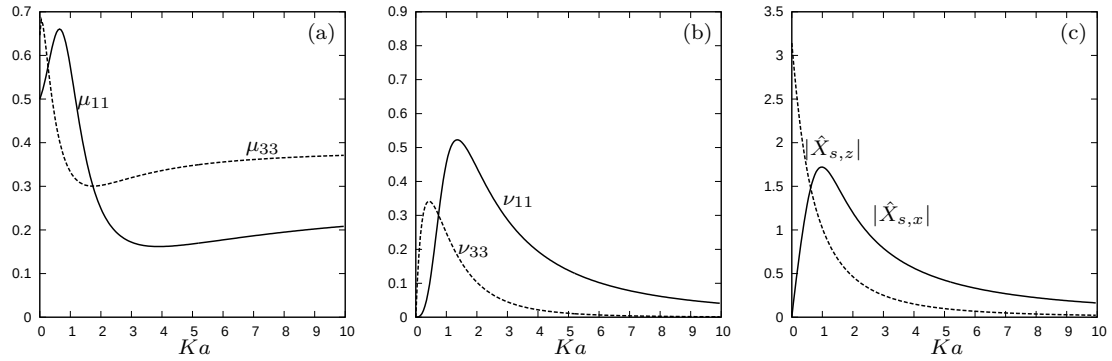

Figure 3: In (a), (b) the non-dimensional added mass and radiation damping coefficients against a dimensionless frequency parameter, Ka, for a surging (solid lines) and heaving (dashed lines) sphere. In (c) the magnitude of the non-dimensional surge (solid) and heave (dashed) wave exciting force.

at the centre and bottom of the sphere to represent the WITT gearbox and power take-off (PTO) machinery and ballast respectively. The centre of gravity of the hull thus lies a distance below the centre of the sphere. Resolving the vertical forces on the sphere and mooring lines determines the mass of ballast required for the device to be semi-submerged when in equilibrium.

3. Mathematical modelling

The mathematical model of the device described in Section 2 can be broken down into three components: (i) the hydrodynamic response of a sphere in waves (described later); (ii) the mathematical model of the mooring system (described in detail in Appendix A); and (iii) the dynamics of the fully coupled mechanical system of sphere - mooring - pendulum (described in detail in Appendix B).

Underpinning each element is a small amplitude assumption, a routine first step in the analysis of WECs as it allows the equations describing the device motion to be linearised and thus solutions can be sought by factorising a time-harmonic variation with radian frequency ω from the dynamic variables. The small amplitude assumption manifests itself in different ways when applied to each of the different elements of the design. Principally, the incident waves which excite the motion are assumed to be of small steepness. We also require device motions to be small enough to justify the use of linearised hydrodynamic theory and linearised elastic behaviour in the mooring model. The response of the internal pendulum must also be of sufficiently small amplitude. These assumptions will all be tested at device resonance which is an integral part of WEC design.

It is shown in Appendix B that the motion can be described by two uncoupled sets of equations. The vertical motion is described by the third equation in (B.15) where $\mathrm{Re}\{V\mathrm{e}^{-\mathrm{i}\omega t}\}$ is the vertical velocity and does not contribute to power production under the small amplitude assumption. The surge and pitch motions of the hull, encoded in the time-independent quantities U and Ω, are coupled to the rotation of the internal pendulum in the equation of motion

$$-\mathrm{i}\omega \mathsf{M}\boldsymbol{U} = \boldsymbol{X}_w - \frac{\mathrm{i}}{\omega}\left(\mathsf{C}+\mathsf{K}\right)\boldsymbol{U} - \gamma \mathsf{G}\boldsymbol{U} \tag{1}$$

(see Appendix B). The complex velocity vector $\boldsymbol{U}$ is given by $\boldsymbol{U} = (U, \Omega, \Omega_r)^T$ where Ω_r encodes the rate of rotation of the pendulum relative to the hull. The inertia matrix M, mass restoring

force matrix C and mooring force matrix K are defined by (B.19) and (B.20) whilst G is also given by (B.20) and is pre-multiplied in (1) by the PTO parameter, γ, which we are free to tune. All matrices are real and symmetric and determined by geometric parameters of the problem. The vector $\boldsymbol{X}_w = (X_{w,x}, 0, 0)^T$ where $X_{w,x}$ is the time-independent surge component of the wave exciting force on the hull. The heave exciting force $X_{w,z}$ is also needed to determine V in (B.15). Both can be decomposed using linearity in the usual way into forces on the static hull and radiation forces due to the motion of the hull. Thus we write

$$X_{w,x} = X_{s,x}\cos\beta + (\mathrm{i}\omega A_{11} - B_{11})U - D_{11}U \tag{2}$$

where β is the incident wave direction and

$$X_{w,z} = X_{s,z} + (\mathrm{i}\omega A_{33} - B_{33})V - D_{33}V. \tag{3}$$

The forces $X_{s,x}$ and $X_{s,z}$ and the added mass and radiation damping coefficients A_{ii} and B_{ii} are calculated here following [11] which assumes water of infinite depth. Note there are no wave forces in the pitch mode of motion owing to the hull being spherical. Forces accounting for hydrodynamic drag resulting from the differential flow between the fluid and the sphere are modelled in (2) and (3) by terms linearly proportional to device velocities and with constants of proportionality D_{11} and D_{33}. A brief description of the derivation of this drag model and estimates to the values of D_{ii} will be discussed later in §3.4.

Tabulated values of the added mass and radiation damping coefficients are provided in [11], but the wave exciting forces are not calculated explicitly. In Fig. 3 the non-dimensional equivalents of these quantities are plotted against the non-dimensional wave frequency $Ka \equiv \omega^2 a/g$, where

$$\mu_{ii} = \frac{A_{ii}}{M_w}, \quad \nu_{ii} = \frac{B_{ii}}{M_w\omega}, \quad \hat{X}_{s,\alpha} = \frac{X_{s,\alpha}}{\rho a^2 \omega}, \tag{4}$$

with $\alpha = x, z$ for surge and heave respectively and where $M_w = \frac{2}{3}\pi\rho a^3$ is the mass of water, density ρ, displaced by the sphere which has radius a.

3.1. Device motion

Using equation (2), the equation of motion (1) can be inverted to give the response as

$$\boldsymbol{U} = \mathsf{E}\boldsymbol{X}_s, \tag{5}$$

where $\boldsymbol{X}_s = (X_{s,x}\cos\beta, 0, 0)^T$,

$$\mathsf{E} = (\mathsf{Z} + \gamma\mathsf{G})^{-1}, \tag{6}$$

and

$$\mathsf{Z} \equiv \mathsf{B} - \mathrm{i}\omega\left(\mathsf{M} + \mathsf{A} - (\mathsf{C} + \mathsf{K})/\omega^2\right). \tag{7}$$

after defining

$$\mathsf{A} = \begin{pmatrix} A_{11} & 0 & 0 \\ 0 & 0 & 0 \\ 0 & 0 & 0 \end{pmatrix}, \qquad \mathsf{B} = \begin{pmatrix} B_{11} + D_{11} & 0 & 0 \\ 0 & 0 & 0 \\ 0 & 0 & 0 \end{pmatrix}. \tag{8}$$

For the heave response, the third equation in (B.15) is similarly used with (3) to give

$$V = \frac{X_{s,z}}{(B_{33} + D_{33} - \mathrm{i}\omega(M + A_{33} - (K_{33} + \rho g S)/\omega^2))} \tag{9}$$

where M and S are defined in Appendix B and K_{33} is defined in (A.14). Subsequently, the sphere and pendulum motions are given by

$$X(t) = \mathrm{Re}\{(gA/\omega^2)U\mathrm{e}^{-\mathrm{i}\omega t}\}, \qquad \Theta(t) = \mathrm{Re}\{(gA/\omega^2)(\Omega/l)\mathrm{e}^{-\mathrm{i}\omega t}\},$$
$$Z(t) = \mathrm{Re}\{(gA/\omega^2)V\mathrm{e}^{-\mathrm{i}\omega t}\}, \qquad \theta(t) = \mathrm{Re}\{(gA/\omega^2)((\Omega+\Omega_r)/l)\mathrm{e}^{-\mathrm{i}\omega t}\}. \tag{10}$$

following (B.14) where A is the wave amplitude, g is gravitational acceleration and l is the natural length of the pendulum, (B.3). Device RAOs (Response Amplitude Operators) are defined as the maximum excursion per unit wave amplitude.

3.2. Power calculation

The mean power (time averaged over a period, $T = 2\pi/\omega$) per unit crest length of an incident wave of amplitude A is given as

$$W_{inc} = \tfrac{1}{2}\rho g|A|^2 c_g \tag{11}$$

where c_g is the group velocity given by $\frac{1}{2}(g/\omega)$ in deep water.

The mean power absorbed by the device is equivalent to the mean rate of working of the wave forces (see Appendix B) against the device motion, that is

$$W = \frac{1}{T}\int_0^T (F_{w,x}(t)\dot{X}(t) + F_{w,z}(t)\dot{Z}(t))\mathrm{d}t$$

and can be expressed, after use of the decomposition in (B.14), as

$$\begin{aligned} W &= \tfrac{1}{2}(g^2|A|^2/\omega^2)\mathrm{Re}\{X^*_{w,x}U + X^*_{w,z}V\} = \tfrac{1}{2}(g^2|A|^2/\omega^2)\mathrm{Re}\{\boldsymbol{X}^*_w\boldsymbol{U}\} \\ &= \tfrac{1}{2}(g^2|A|^2/\omega^2)\mathrm{Re}\{\gamma\boldsymbol{U}^*\mathsf{G}\boldsymbol{U}\} \\ &= \tfrac{1}{2}(g^2|A|^2/\omega^2)\mathrm{Re}\{\gamma|\Omega_r^2|\} \end{aligned} \tag{12}$$

where * denotes the complex conjugate transpose. In the above the third equation in (B.15) is used with (1) and the fact that the elements of M, K and C are all real. We recognise the last equation in (12) as the mean power developed by the rotation of the pendulum relative to the sphere, that is

$$W = \frac{1}{T}\int_0^T \gamma l^2(\dot{\theta} - \dot{\Theta})^2\mathrm{d}t.$$

As expected we have demonstrated the equivalence of the power generated by the waves acting on the hull to the power generated by the PTO machinery.

Using (11) in (12) we can define the capture width as

$$l(T,\beta) = \frac{W}{W_{inc}} = \frac{g}{\rho\omega^2 c_g}\mathrm{Re}\{\gamma|\Omega_r|^2\} \tag{13}$$

being the equivalent length of incident wave from which all energy is absorbed. Assuming a fixed power take-off parameter, γ, the capture width is a function of wave period, T, and wave heading, β. Although (13) can be computed in the form presented further useful progress can be made.

We denote the i,jth element of E defined in (6) by E_{ij}/Δ where $\Delta = \det(\mathsf{E})$ and the i,jth element of Z defined in (7) by Z_{ij}. Since $(\mathsf{Z}+\gamma\mathsf{G})\mathsf{E} = \mathsf{I}$, the 3×3 identity matrix, it follows that

$$\Delta = E_{33}\left(\gamma + Y\right). \tag{14}$$

where

$$Y = Z_{33} + \left(Z_{13}E_{13} + Z_{23}E_{23}\right)/E_{33} \tag{15}$$

which, crucially for what follows, is independent of γ since

$$E_{13} = Z_{12}Z_{23} - Z_{13}Z_{22}, \qquad E_{23} = Z_{13}Z_{12} - Z_{11}Z_{23}, \qquad E_{33} = Z_{11}Z_{22} - Z_{12}^2. \tag{16}$$

From (5), $\Omega_r = (E_{13}/\Delta)X_{s,x}\cos\beta$ and so (13) becomes,

$$l = \frac{g}{\rho\omega^2 c_g}\mathrm{Re}\left\{\frac{\gamma|X_{s,x}|^2|E_{13}|^2\cos^2\beta}{|E_{33}|^2|\gamma+Y|^2}\right\} \tag{17}$$

after using (14). The Haskind relation (e.g. see [8]) provides the following

$$B_{11} = |X_{s,x}|^2/(8\rho c_g) \tag{18}$$

which allows (17) to be written as

$$l = \frac{8B_{11}}{K}\mathrm{Re}\left\{\gamma\frac{|E_{13}|^2\cos^2\beta}{|E_{33}|^2|\gamma+Y|^2}\right\}. \tag{19}$$

where $K = \omega^2/g = 2\pi/\Lambda$ and Λ is the incident wavelength. If we assume γ to be real we can use the general identity,

$$\frac{2\gamma}{|\gamma+Y|^2} = \frac{1}{(|Y| + \mathrm{Re}\{Y\})}\left(1 - \frac{(\gamma-|Y|)^2}{|\gamma+Y|^2}\right), \tag{20}$$

as in [9] allowing us to rewrite (17) as,

$$l = \frac{2\Lambda B_{11}|E_{13}|^2\cos^2\beta}{\pi|E_{33}|^2\left(|Y| + \mathrm{Re}\{Y\}\right)}\left(1 - \frac{(\gamma-|Y|)^2}{|\gamma+Y|^2}\right). \tag{21}$$

From (15), considerable algebra leads to the relation

$$\mathrm{Re}\{Y\} = \frac{(B_{11}+D_{11})|E_{13}|^2}{|E_{33}|^2} \tag{22}$$

which, when used in (21), gives our final expression for the capture width as

$$l(T,\beta) = \frac{\Lambda}{\pi}\frac{B_{11}}{(B_{11}+D_{11})}\frac{2\mathrm{Re}\{Y\}}{(|Y| + \mathrm{Re}\{Y\})}\left(1 - \frac{(\gamma-|Y|)^2}{|\gamma+Y|^2}\right)\cos^2\beta. \tag{23}$$

Thus, the original expressions for the mean absorbed power given in (12) has been reduced to (23) with $W = lW_{inc}$ and the dependence on the PTO parameter, γ, has been made explicit in the final bracket of equation (23). Consequently the power is maximised, when $\gamma = |Y|$ and the hydrodynamic damping $D_{11} = 0$, to the value which we will call the optimal capture width and label

$$l_{opt} = \frac{\Lambda}{\pi}\frac{2\mathrm{Re}\{Y\}}{|Y| + \mathrm{Re}\{Y\}}\cos^2\beta. \tag{24}$$

(a) 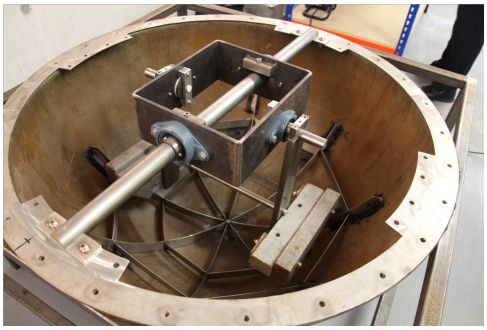 (b) 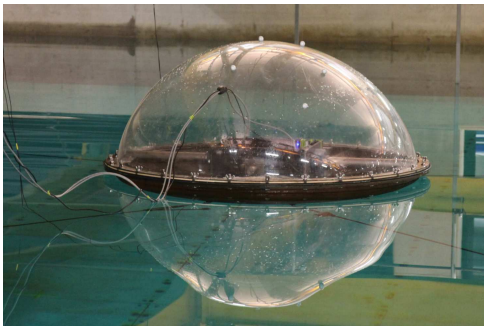

Figure 4: Images of the experimental set up: In (a) the internal arrangement of the sphere used in the experimental tests and (b) the sphere, semi-submerged in calm water, during tank testing.

If, additionally, $\mathrm{Im}\{Y\} = 0$, then

$$l_{opt} = l_{max} \equiv \frac{\Lambda}{\pi} \cos^2 \beta \tag{25}$$

which is the maximum theoretical capture width that a vertically axisymmetric wave power device operating in surge/pitch can achieve, a well-known result – see [8] or [13].

In other wave energy problems with simpler mechanical components it is easy to identify the condition under which $l_{opt} = l_{max}$ with a resonant condition being met (e.g. [9]). Often this is a balance between inertia – including hydrodynamic inertia – and spring forces. Because of the complexity of Y in (15) it seems unlikely that a similar connection can be made here. However, by analogy with these simpler systems we will refer the condition for device resonance as $\mathrm{Im}\{Y\} = 0$ at which $l_{opt} = l_{max}$. We recall the tuning condition for optimal power is $\gamma = |Y|$ when $l = l_{opt}$. Thus if both tuning and resonance conditions are satisfied at the same frequency, $l = l_{max}$.

We remark that for axisymmetric devices taking power in heave only l_{max} is half that reported above whilst a device capable of taking power in both surge/pitch and heave motions the value of l_{max} reported above is increased by a factor of 1.5 ([8] or [13]).

3.3. Non-dimensionalisation

In order to solve (5) we define dimensionless variables using $\hat{Z} = Z/(M_w\omega)$, $\hat{\boldsymbol{X}}_s = a\boldsymbol{X}_s/(M_w\omega)$, $\hat{\boldsymbol{U}} = a\boldsymbol{U}$ and $\gamma/(M_w\omega) = \hat{\gamma}/\sqrt{Ka}$ so that a fixed $\hat{\gamma}$ implies a fixed physical PTO damping constant, γl^2.

Consequently the RAOs in surge and heave are defined from (10) as dimensionless quantities $\mathcal{X} = |\hat{U}|/Ka$ and $\mathcal{Z} = |\hat{V}|/Ka$ and the hull pitch and pendulum RAOs are $\vartheta = |\hat{\Omega}|/(Kal)$ and $\vartheta_p = |\hat{\Omega} + \hat{\Omega}_r|/(Kal)$ and are not dimensionless, but measured per metre of wave amplitude.

Results presented later will be expressed in terms of dimensionless capture width ratios – or capture factors – where capture widths are divided the by the device diameter, $2a$. These are defined as $\hat{l} = l/2a$, $\hat{l}_{opt} = l_{opt}/2a$ and $\hat{l}_{max} = \Lambda \cos^2 \beta/(2\pi a)$ These are all frequency and incident angle dependent and should not be confused with the *mean* capture factor $\bar{l}$ (defined in §5) which encodes the similar information but is averaged over all incident frequencies and angles.

3.4. Hydrodynamic drag

We assume that the total hydrodynamic drag is dominated by turbulent drag and adopt, as a starting point, a quadratic law to capture its effect. For surge motions, this drag force is approxi-

mated by $\frac{1}{2}\rho C_D \mathbb{A}\dot{X}(t)|\dot{X}(t)|$ where $C_D \approx \frac{1}{2}$ is the drag coefficient for a sphere and $\mathbb{A} = \frac{1}{2}\pi a^2$ is its frontal area. This approximation neglects the effect of background flow velocity. Using the Lorentz principle of equivalent work over a cycle, the linearised version of this drag is $4\rho C_D \mathbb{A} A\omega U/(3\pi)$ and this, with reference to (2), gives $D_{11} = 4\rho C_D \mathbb{A} A\omega/(3\pi)$ having assumed a characteristic device velocity based on the background wave field. The dimensionless drag coefficient is therefore

$$\hat{D}_{11} = D_{11}/(M_w\omega) \approx 0.16A/a. \tag{26}$$

Dedicated experimental studies, beyond the scope of the current project, can be used to parametrise $\hat{D}_{11}$ accurately and (26) should be regarded only as a simple first attempt at capturing the correct order of magnitude of the drag effects.

For example, with 2m wave amplitude and a 7.5m diameter sphere, $\hat{D}_{11} \approx 0.04$ and it can be seen from Fig. 3 that this is small percentage of $\nu_{11} = B_{11}/(M_w\omega)$ to which $\hat{D}_{11}$ is added in calculations (equations (8), (23)).

Although heave motion is affected by drag, it does not contribute to power absorption and hence we do not consider the influence of D_{33} here.

Because of the uncertainty with setting an accurate representation of drag, all calculations in the main results section are made with $D_{11} = 0$. That is, we do not want to misrepresent our results or analysis. However, some brief comments on the effect of including drag into the calculations are made in the Conclusions.

4. Prelimary model validation with experimental results

Scale tank test experiments were conducted in the UK's Plymouth University ocean wave basin, in order to validate the RAOs of the device predicted by the mathematical model.

The following experimental set-up was chosen. A 1.2m diameter spherical hull was constructed from bolting a lower hemisphere made of steel to an upper hemisphere of perspex allowing observations of the pendulum motion to be made. The hull contained a simplified pendulum model of the WITT as no suitable WITT unit was available for testing. Two pendulums were suspended and free to move independently about a single common axis perpendicular to the incident wave direction, see Fig. 4(a). Observations made during the tests confirmed motions of the two pendulums were synchronised. No rotation was allowed about the the transverse axis, as per assumptions in the analysis. No power take-off device was attached to the pendulums.

The hull was moored to the bottom of the wave tank (which was filled to a depth of 3m) using pre-tensioned elastic bungee cord. Sufficient lead ballast was placed at the bottom of the hull to ensure near semi-immersion of the hull, see Fig. 4(b). The sphere was raised about 50mm above the level of semi-immersion to help mitigate against the effects from the protruding lip of the sphere formed where the upper and lower sections were bolted together. Four elastic cords were splayed symmetrically left and right and fore and aft of the hull and pre-tensioned according to the model outlined in Appendix A. Small variations (less than 5%) in the pre-tensioning in each cord was required to configure an aligned and level static configuration which suppressed unwanted yaw and roll effects in motion. These adjustments were needed to account for small misalignments in the positioning of eye-bolts on the sphere for the mooring line attachments. Static loadings were applied to the bungee cord to determine its elastic modulus and confirm that the behaviour of the cord in motion was Hookean.

Some of the modelling outlined in the main body of the paper has been altered to reflect the experimental model. This involved the use of the elastic mooring model, described at the end of

Appendix A and the setting of the PTO parameter γ to zero in addition to determining appropriate moments of inertia and centres of gravity specific to the experimental model.

Tests were run across a range of single wave frequencies, with particular focus around the resonant frequency of the internal pendulum. These tests were repeated at three different wave amplitudes: 50mm, 100mm and 200mm. All tests were performed with normally-incident waves.

The experimentally measured device RAOs are plotted in Fig. 5 using symbols, along with the output from the mathematical model (with damping $D_{11} = 0$) using solid lines. The root mean square (RMS) surge and heave values have been non- dimensionalised by the RMS wave amplitude and the pitch and pendulum RMS values, measured in radians, have been normalised by the non-dimensional RMS wave steepness, $\omega^2 A/g$ in order to obtain the RAOs.

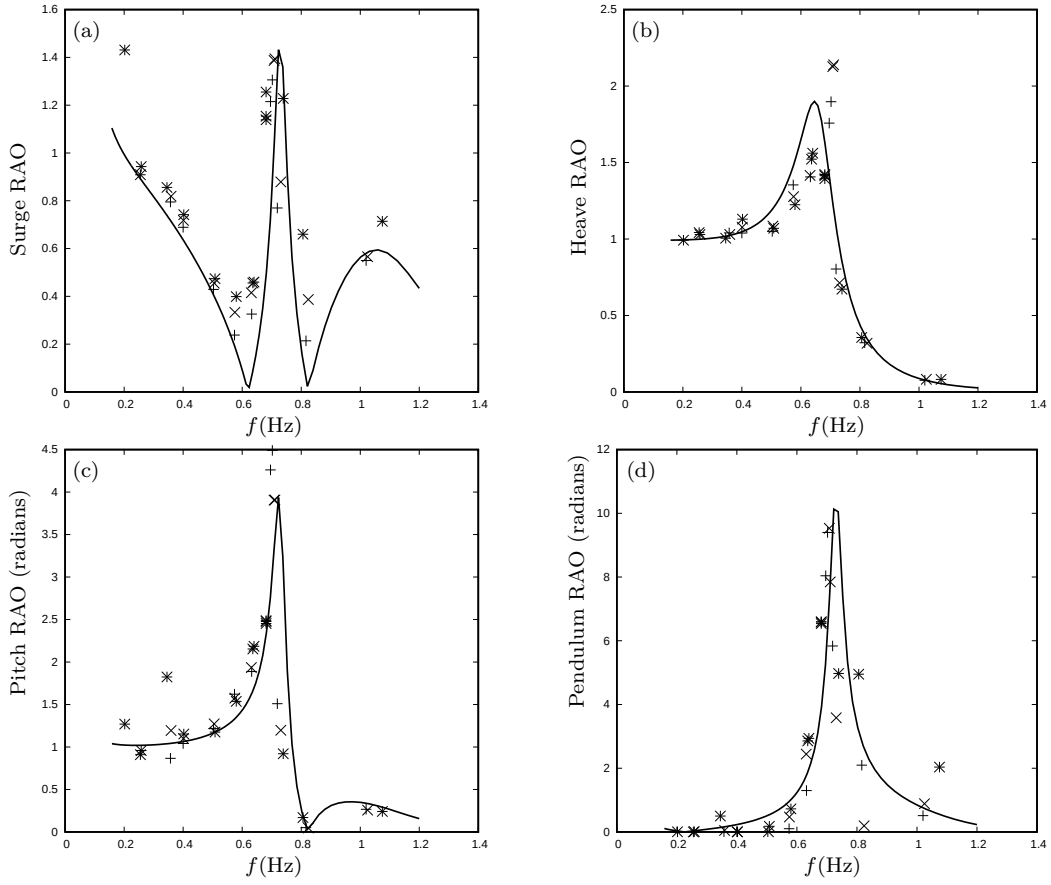

Figure 5: Comparison of the theoretical (line) and experimental (points) results for (a) surge, (b) heave, (c) pitch and (d) relative pendulum RAOs against wave frequency in Hertz. The different symbols represent results from different incident wave amplitudes used in the experiments: $A = 50$mm (+); $A = 100$mm ($\times$) $A = 200$mm ($*$).

Generally, the results show good agreement. The frequency of the resonant peak is offest very slightly between experiments and theory and this is probably due to small errors made in estimating measurements of the hull/ballast/pendulum/mooring configuration. The experiments also demonstrate that the response of the buoy and the pendulum is generally linear with increasing

$h = 3\text{m}$	$T_0 = 70\text{N}$	$m_s = 75\text{kg}$
$a = 0.6\text{m}$	$L_0 = 8.4\text{m}$	$I = 211\text{kgm}^2$
	$\lambda = 150\text{N/m}$	
$\alpha = 48.2°$		$m_b = 309\text{kg}$
$\chi = 71.3°$	$l = 0.335\text{m}$	$L = 0.44\text{m}$
$\eta = 67.5°$	$m = 77\text{kg}$	
$\zeta = 34.4°$	$mk^2 = 9.5\text{kgm}^2$	$M = 452\text{kg}$

Table 1: Table of measured and calculated experimental parameters used to generate data and curves in Fig. 5.

wave height and it is only at the highest wave amplitude of 200mm (so that the wave height is one third of the hull diameter) is there any notable difference. Here the resonant peaks in RAOs drop significantly lower than for the two other wave heights. The inclusion of a linear damping term using (26) in the theoretical model reduces the peak response in the surge and pendulum motions for the largest 20mm wave amplitudes by roughly 8% whilst the response elsewhere changes very little. Thus, it seems that hydrodynamic drag is not an important factor in these experiments. Other non-linear effects may be influential. For example, for the largest 200m wave amplitudes linear theory predicts a pendulum amplitude of 43° at peak resonance, around 0.73Hz. The time series from the experimental results for these largest waves revealed that the pendulum motion became asymmetric around the peak resonant frequency (the most extreme records showing motions between $-20°$ and 50° for the relative motion of the pendulum against the hull). The displayed experimental results have been adjusted to account for this offset in the mean position of the motion. The non-linear effects described above may have been caused by a lip around the equator of the hull (Fig. 4) which was observed to slam hard against the water surface especially at resonance in larger amplitude waves.

Similar results, not shown here, have been obtained for a different splay and pre-tensioning of mooring lines with similar agreement observed.

The generally good correlation between theory and experiments provide us with confidence that the theoretical model can make reasonable predictions about a full scale WITT WEC apart from at the largest amplitudes. In particular, experiments have indicated that predictions using linear theory of pendulum pitch motions beyond roughly 30° show a loss of accuracy and this will act as an important guide later.

5. Optimisation of full scale devices

In order to demonstrate the efficacy of the proposed design, we set out to optimise the device performance over a wave energy spectrum for a given device test site. We have considered the Billia Croo EMEC test site, on the western edge of the UK's Orkney mainland. For context, the EMEC site has an annual average wave power of 21kW/m and an average water of depth 50m, justifying the earlier deep water modelling assumptions in the calculation of the hydrodynamic coefficients.

A scatter diagram of probabilities of expected sea states is replicated in Fig. C.12 but can also be found in [14], allowing us to define a joint probability function $P(H_s, T_p)$ of the likelihood of occurrence of a pair of parameter values describing a particular sea state, where H_s is the significant wave height and T_p the peak wave period.

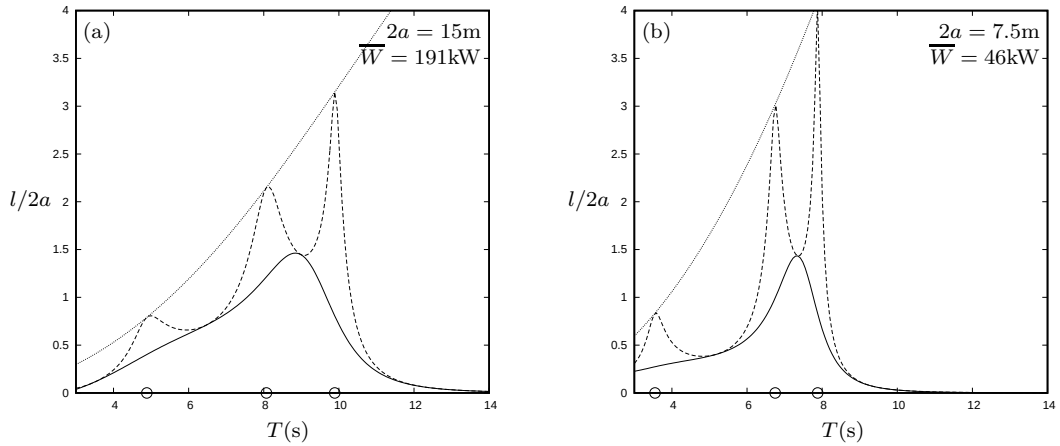

Figure 6: Maximum (dotted), optimum (dashed) and achievable (solid) capture width ratio for a device of diameter (a) $2a = 15$m and (b) $2a = 7.5$m, under head seas. The circles indicate periods at which $\mathrm{Im}\{Y\}$ vanishes.

We employ the two parameter spectrum developed by [3] and using the probability function $P(H_s, T_p)$ along with a function $G(\theta)$ to describe the angular spread of the energy density of the incident wave field, define a modified spectrum, $\tilde{S}(T, \theta)$. Expressions for these functions can be found in Appendix C, equations (C.1)–(C.3).

The total mean power absorbed by a device of width $2a$ is then

$$\overline{W} = \rho g \int_{-\pi}^{\pi} \int_{0}^{\infty} c_g(T) \tilde{S}(T, \beta) l(T, \beta) T^{-2} \, \mathrm{d}T \, \mathrm{d}\beta, \tag{27}$$

where $l(T, \beta)$ is given in (23) and $c_g = Tg/4\pi$ in deep water. The explicit $\cos^2 \beta$ variation in l in (23) combined with the model spread in (C.3) allows the β dependence (27) to be integrated analytically to 25/26. Thus, only integration over period is required and multiplication by 25/26 accounts for spreading.

We can also define a dimensionless *mean* capture factor,

$$\overline{l} = \frac{\overline{W}}{\overline{W}_{inc} 2a}, \tag{28}$$

which describes the mean proportion of incident wave power absorbed per unit width of the device, where $\overline{W}_{inc}$ has been defined in (C.5).

With many free parameters in this problem, we employ a numerical optimiser from the NAG library (E04JYF) to determine the design parameter values which maximise the mean capture factor, $\overline{l}$, over a given wave energy spectrum. In order to reduce the numerical effort required, a small number of parameters are fixed: for example, the density of the pendulums are set to that of concrete and the spherical structure is assumed to be equivalent to a shell of thickness 0.001% of the sphere diameter (e.g. 10mm for a 10m sphere) and to be made of steel. Upper and lower bounds are also imposed on the optimisers free parameters to ensure that optimised configurations are physically sensible. These include bounds on the inclination of the mooring lines, the slack in the static mooring line configuration and the position of masses along the mooring line. Some of

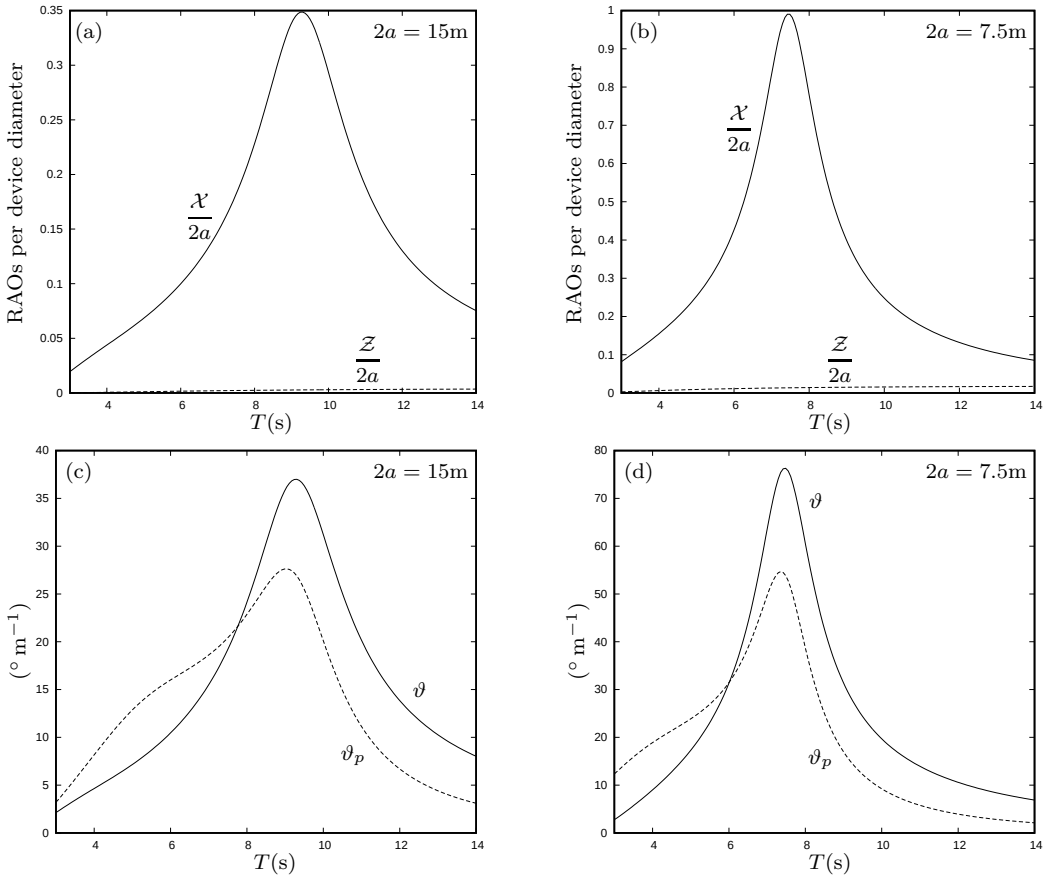

Figure 7: The RAOs in surge, $\mathcal{X}$ (solid lines), and heave, $\mathcal{Z}$ (dashed lines), per device diameter for (a) 15m and (b) 7.5m diameter WITT WECs; the angular pitch, ϑ (solid lines), and pendulum, ϑ_p (dashed lines), RAOs, for (c) 15m and (d) 7.5m diameter WITT WECs

these have been guided by advice from marine engineers employed as part of the current project. This includes weights of mooring lines.

In Fig. 6 curves of the theoretical maximum, the optimal and the actual capture width ratio (i.e. for fixed PTO parameter) plotted for two numerically optimised WITT WEC devices of 15m and 7.5m diameter.

In both plots, the optimal capture width ratio $l_{opt}/2a$ possess three peaks which extend to the theoretical maximum. As noted in Section 3.2, these peaks are associated with the resonant condition $\mathrm{Im}\{Y\} = 0$, which are indicated in Fig. 6 by the circles on the period axis.

The numerical optimisation has distributed these resonances across the range of periods and selected the particular PTO parameter, γ, such that the realisations given by the solid curves maximises the mean power, $\overline{W}$, (i.e. averaged over the wave energy spectrum). Those values are indicated within the figures. The multiple resonances can be seen to broaden the capture width ratio over a range of wave periods so that, for example, for the 15m device, the capture width ratio,

	Unconstrained		Case (i)		Case (ii)	
Diam.	$\overline{W}$	$\overline{l}$	$\overline{W}$	$\overline{l}$	$\overline{W}$	$\overline{l}$
6	27	0.22	22	0.17	14	0.12
9	70	0.37	63	0.34	57	0.31
12	127	0.51	122	0.49	115	0.46
15	191	0.61	190	0.61	183	0.59
18	258	0.69	258	0.69	254	0.68
21	325	0.74	325	0.74	325	0.74
24	387	0.77	387	0.77	387	0.77

Table 2: Table of mean capture factor $\overline{l}$, and mean power $\overline{W}$ (kW) for different diameters (m) with and without motion constraints.

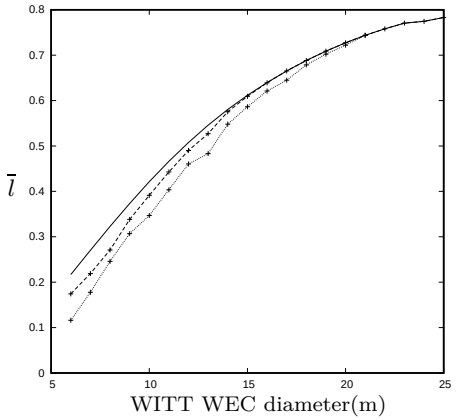

Figure 8: Mean capture factor against device size: Unconstrained (solid); Case (i) (dashed); Case (ii) (dotted).

$l/2a$, is greater than unity across 8–10s waves and is above a half for a 5-second range of wave periods. These ranges are smaller for the half-size 7.5m device, as might be expected. The other effect of the optimisation is that it selects a configuration and PTO characteristics which smooth out the power capture over the range of wave periods. In other words the device de-tuned away from the peak resonances, but is near resonant over a broad range of periods instead. This, in turn, also helps smooth out the RAOs and the loads on the mooring.

Selecting other non-optimal fixed values of PTO parameter, γ, shifts the solid curve around under the optimal curve resulting in lower overall mean power, $\overline{W}$. This procedure has a useful purpose, allowing us to tune the device to the each of the three resonant peaks in turn as a means of understanding the characteristic device behaviour associated with these resonances. Thus, the lowest resonant period is found to be associated with a resonant motion of the pendulum only. This tallies with (B.5) which provides the natural resonant period of the pendulums in isolation for the two optimised 15m and 7.5m spheres as 5.29s and 3.79s, close to the values indicated on the horizontal axis. The other two peaks at higher periods excite large motions in all three components of pendulum, WEC pitch and surge motions. This is reminiscent of the effects observed in 'tuned mass dampers' (see, for example, [12]) where the coupling of different independent motions leads to bifurcation of resonances. Under linear theory heave is decoupled from pitch, surge and pendulum rotation and consequently no resonant heave motions are observed in any results.

The RAOs corresponding to the optimised solid curves in Fig. 6 are given in Fig. 7. They show, respectively, the surge and heave RAOs per device diameter and the angular RAOs of the internal pendulum and pitch of the device, measured in degrees per metre wave amplitude (see §3.3). The RAOs for the 7.5m sphere are more than double that for the 15m sphere. This is not surprising (indeed, it is well known) that smaller devices optimised to maximise power output have larger responses than larger devices; see [7] for example. We notice that the heave motion is very small in both cases; this is in part due to the optimal mooring line configuration which nearly always favours the steepest allowable mooring angle (30° to the vertical in our design space) at the point of attachment to the sphere. The surge RAO for the 15m optimal design is not exceptionally large. However, the pitch and pendulum RAOs suggest that linear theory could only be expected to hold

in low to moderate wave heights. The 7.5m optimal design has RAOs which are well outside the range of validity of linear theory apart from in low seas.

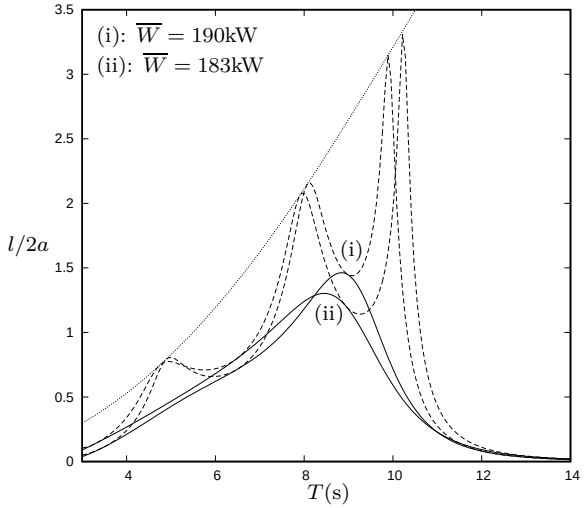

Figure 9: The maximum (dotted), optimal (dashed) and actual (solid) capture width ratios for a 15m diameter WITT WEC optimised under Case (i) and (ii) motion constraints.

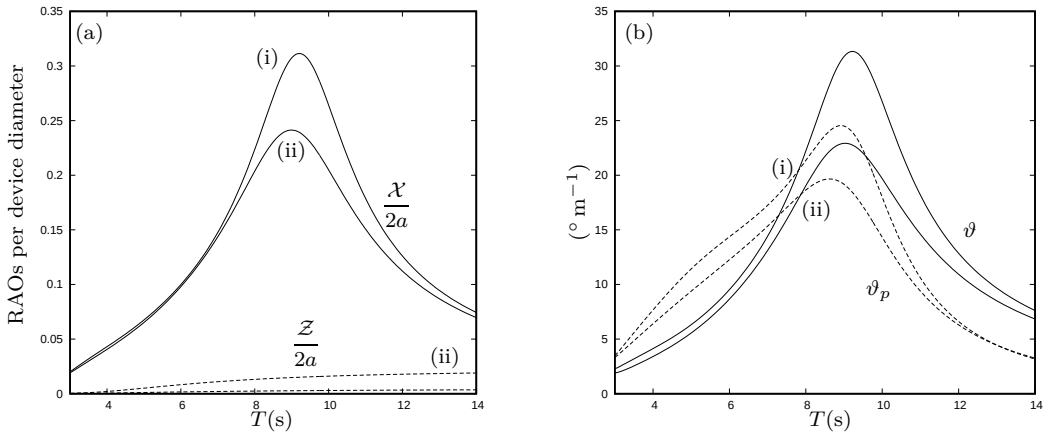

Figure 10: RAOs for 15m diameter WITT WEC optimised under motion constraints Case (i) and (ii): (a) surge, $\mathcal{X}$ (solid lines), and heave, $\mathcal{Z}$ (dashed lines) measured per device diameter and (b) the pitch, ϑ (solid lines), and pendulum rotation, ϑ_p (dashed lines) measured in degrees per metre wave amplitude.

5.1. Optimisation with motion constraints

Theoretical work to include the effect of motion constraints on power output have been considered in, for example, the work of [7] and [15]. In Fig. 1 of [7] it was shown that restricting the vertical motion of a heaving semi-immersed spherical WEC to different proportions (results for 0.5,

1 and 2 are shown) of the wave amplitude leads to a reduction in the capture width ratio from its maximum $\Lambda/2\pi$ for unconstrained motions as Λ increased.

We have not attempted to follow [7] and apply theoretical motion constraints here. Since a numerical optimisation is already being used with constraints on input design parameters, we have considered restricting the output RAOs as part of the optimisation. This is done by including a smooth penalty function into the optimiser's objective function which is set to penalise motions above threshold which can be set arbitrarily.

As an illustration, each WEC size has been optimised in the same manner as before but subject to two different sets of constraints, one more severe than the other. In Case (i) the penalty threshold of heave and surge RAOs is set at the half the device diameter, and the pendulum and hull pitch RAOs set at 30° per metre wave amplitude (i.e. per 2m wave height). Case (ii) restricts heave and surge RAOs to 25% of device diameter and angular rotations to 22.5° per metre wave amplitude. These are somewhat arbitrary, although they are influenced by the range of validity indicated by the experimental results and the distribution of significant wave heights at the EMEC test site, Fig. C.12. Moreover, they provide a good indication of the effects that motion constraints introduce.

Numerical results are presented in Table 2 and Fig. 8 for the mean power and the capture width ratios for both constrained cases alongside the unconstrained device motion. The optimiser finds it less easy to converge to an optimal solution when a penalty function is introduced and the data for Cases (i) and (ii) is not particularly smooth as a result.

The results demonstrate that motion constraints increase the percentage loss in power as the device gets smaller. Thus, Case (ii) constraints applied to a 6m device leads to roughly a 50% loss in power. However, for larger devices the loss incurred by imposing motion constraints is actually quite small, and for devices larger than 18m optimised motions fall within the bounds of both Case (i) and (ii) constraints.

For devices smaller than 6m the motion constrained devices generate very little power, suggesting that linear analysis is not a useful tool for analysing and optimising smaller devices. This adds to the fact that we have neglected drag forces and these play an increasingly prominent role in smaller devices.

			Case (i)			Case (ii)		
Hull diam. (m)	S. area (m^2)	Mass (t)	$\overline{l}$	$\overline{l}_s$	$\overline{l}_m$	$\overline{l}$	$\overline{l}_s$	$\overline{l}_m$
6	56.54	57.95	0.17	3.53	**3.33**	0.12	2.16	2.11
9	127.2	195.6	0.34	4.33	2.82	0.31	3.92	**2.55**
12	226.2	463.7	0.49	**4.72**	2.30	0.46	4.45	2.17
15	353.4	905.7	0.61	4.70	1.83	0.59	**4.53**	1.77
18	508.9	1595	0.69	4.44	1.41	0.69	4.44	1.41

Table 3: Alternative measures of device performance based on [2] for devices optimised under Case (i) and (ii) motion constraints: annual absorbed energy per submerged surface area $\overline{l}_s$ (Mwh/m^2) and per displaced mass $\overline{l}_m$ (Mwh/t).

Results are only now plotted in Fig. 9 and Fig. 10 for the 15m device under Case (i) and (ii) motion constraints. Although there is only a small reduction in overall mean power, Fig. 9 illustrates the fairly significant shift in the capture width ratios between Cases (i) and (ii) which are broader and lower in the latter. The result of this on the RAOs is evident in Fig. 10. The Case (i) curve

in Fig. 10(b) has the $30^\circ\,\mathrm{m}^{-1}$ threshold imposed and Case (ii) curves are limited by the 0.25 surge RAO limit and the $22.5^\circ\,\mathrm{m}^{-1}$ pitch and and pendulum limit.

In summary, for the 15m device, the optimisation under Case (ii) constraints has resulted in a reduction of under 5% in mean power which has required a reduction in maximum RAOs of $30-40\%$.

The capture factor is arguably not the most appropriate measure for the comparison of the relative performance of WECs of different sizes, especially for a spherical device. [2] suggests some alternative measures, including the annual absorbed energy per characteristic submerged surface area, $\overline{l}_s$, and per characteristic mass, $\overline{l}_m$. These measures are shown for the 6m–18m devices subject to optimised Case (i) and (ii) motion constraints in Table 3. Here, we have defined the characteristic mass as the hull displacement. Unlike the capture factor which is seen to increase as the device size increase, both of these alternative measures take their maximum at intermediate diameters.

Based on Case (i) motion constraints the results in Table 3 might suggest a roughly 9m sphere to be most favourable. Under more plausible Case (ii) motion constraints, the measures perhaps favour a slightly larger device, roughly 12m in size.

6. Conclusions

In this paper we have outlined a mathematical model of a novel design of wave energy converter (WEC) in which a sealed hull containing a heavy pendulum representative of the WITT energy harvesting device operates on the surface of the ocean. The modelling has been carried out using small amplitude theory and care has been taken in the results to assess the WEC performance under the conditions assumed in the model. Furthermore, experimental results have confirmed the key elements of the WEC operation predicted by the theory: the coupling of device motions with an internal pendulum under a four-point mooring system, as assumed in the model.

The derivation of model mooring systems and the equations of motion along with key results of the hydrodynamic modelling are all provided in the paper. The main part of the paper focusses on a derivation of an analytic expression for the capture width which have allowed us to both understand the operation of the WITT WEC and perform rapid computations in numerical optimisation over many device design parameters under a model wave climate. In particular, the ability to be able to calculate the maximum achievable power and its corresponding power take off tuning condition has also allowed us to identify how the system operates, by spreading three resonances across a range of periods allowing broad banded power capture characteristics to be obtained with a smooth RAO response.

Numerical results have focussed on numerically optimised design of WITT WECs with diameters between 6m and 24m operating in the EMEC test site in Orkney, UK. The optimisation is performed over many free parameters of the design including the pendulum shape and mooring configuration and allows thresholds on the motions of elements of the design to be set to ensure the underlying small amplitude theory is not compromised. The imposition of motion constraints to limit the RAOs to operating conditions in all but very heavy seas to ensures that the model assumptions have not been violated and means that the mean power estimates provided for different device diameters are realistic. In illustrative calculations we have focussed on a 15m device, which has been estimated to produce an annual mean power output of 188kW under motion constraints in the 21kW/m wave climate of EMEC, equivalent to a mean capture factor of 0.59.

According to Fig. 16 of [1] such a predicted device performance competes favourably amongst existing WEC designs especially considering it does not technically belong in the the class of oscil-

lating wave surge converter which emerge from the study of [1] as on average the best performing WEC.

However, we have not included effects of hydrodynamic drag (which [1] does by using a quadratic drag law and solving in the time domain) or mechanical losses into our device operation and this will have some impact on its performance. Computations which include a linearised hydrodynamic drag term with the definition (26) in the numerical optimisation without motion constraints show, for example, show the following reduction in mean power: from $\bar{W} = 27$kW to $\bar{W} = 17$kW for a 6m sphere (with $\hat{D}_{11} = 0.075$); from $\bar{W} = 191$kW to $\bar{W} = 167$kW (or $\bar{l} = 0.53$) for a 15m sphere (with $\hat{D}_{11} = 0.030$); from $\bar{W} = 383$kW to $\bar{W} = 363$kW (or $\bar{l} = 0.72$) for a 24m sphere (with $\hat{D}_{11} = 0.018$). Additionally the power take off (PTO) model assumed here is idealised; it includes no mechanical or electrical losses and may not be representative of a practical implementation. Modifications to account for these factors including the influence of random seas, will require further modelling beyond the current first order model most likely performed in numerical time domain simulations and experimental tests.

In the Introduction we highlighted the SEAREV as being a comparable device, employing a counterweight in a sealed hull. In [5], the SEAREV G1 design with roughly the same displacement as a 15m WITT WEC is reported to produce a mean power of 70kW in a wave resource of 25kW. Its width is 14m and the figures above equate to a mean capture factor of $\bar{l} \approx 0.2$.

Although not reported in any detail here, other hull geometries have been considered to investigate whether any significant improvement in the mean absorbed power could be made including: (i) an upright cylindrical hull floating in the surface and moored using the same four-point mooring system as the spherical hull; and (ii) a submerged spherical hull moored to the sea bed via taut lines held under tension by the assumed buoyancy of the hull. Both designs have been modelled using the same underlying principles and assumptions as for the original spherical hull. The performance of each design has been optimised in a similar manner to that described here. Results suggest that there is little difference in the predicted power output from the mathematical model at the scale of 10m–25m diameter device where the small amplitude assumptions can be reasonably applied.

Appendix A. Mooring model

In this Appendix, two different mooring models are outlined. In the first, a simple mathematical model of a four-point heavy catenary mooring system is described, in which a point mass is placed some distance along each of the light, inextensible mooring lines connecting the hull to the sea bed. In the second, taut elastic mooring lines replace the caternary lines: this has been introduced to mimic the experimental set-up. Both models are illustrated in Fig. A.11.

In both cases, it is assumed that the mooring limbs are arranged symmetrically about the sphere, their horizontal projection making an angle ζ to the primary incident wave direction. The mooring points on the spherical hull are described by the two angles α and η as showin in Fig. A.11. The vertical distance from the point of attachment to the seabed is given by $h_1 = h - a\cos\alpha$, (h is the water depth and a is the radius of the hull) and the horizontal distance along the mooring line between these two points $h_2 = h_1 \tan\chi$ so that χ is the angle that the imaginary line from the points of attachment on the hull to the bed make with the vertical. We shall assume that all angles α, η, ζ and χ are given, in addition to h and a.

The hull can move along the horizontal x axis by $X(t)$ (surge) and along the vertical z axis by $Z(t)$ (heave) and it can rotate by an angle $\Theta(t)$ about the y-axis (pitch, measured clockwise). As it moves in each of these three modes of motion, the tension in each of the four mooring lines

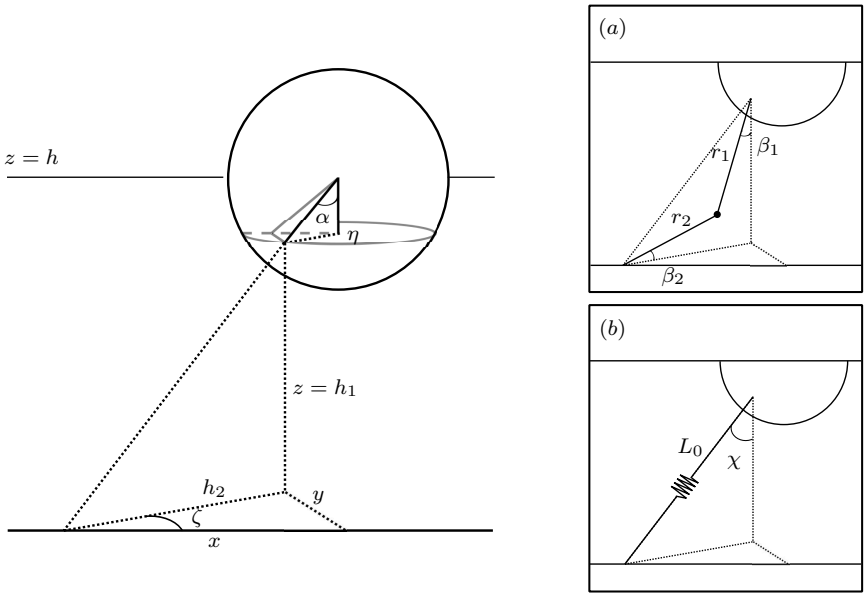

Figure A.11: A basic definition sketch of a single mooring limb of the four point mooring system in (a) the catenary type mooring system, in (b) the taut, extensible mooring system.

attached to the hull will also change and this will provide reactive force/moments on the hull. It is the relation between the motion and these force/moments we set out to derive here.

Appendix A.1. Catenary mooring system

Each mooring limb comprises two straight, massless, line segments of fixed lengths r_1 and r_2 with a single point mass m_l at their intersection, see Fig. A.11(a). The ratio $\hat{r} = r_1/r_2$ is assumed to be a given mooring parameter, as is m_l.

Consider just one mooring limb connected to the hull. The tension in the upper segment is denoted T_1 in Fig. A.11 and so the components of the tension in the x and z directions are

$$T_{1x} = T_1 \sin\beta_1 \cos\zeta, \qquad T_{1z} = T_1 \cos\beta_1, \tag{A.1}$$

along with the pitch moment about the centre of the sphere,

$$M_{1\theta} = T_1 a \left(\cos\eta \sin\alpha \cos\beta_1 - \cos\zeta \cos\alpha \sin\beta_1\right), \tag{A.2}$$

which, we note, may be written

$$M_{1\theta} = a \left(T_{1z} \cos\eta \sin\alpha - T_{1x} \cos\alpha\right). \tag{A.3}$$

Additionally there is a component of tension in the y direction and yaw and roll moments non of which contribute to the dynamics.

When the hull is in motion, Cartesian components of distance between the mooring points on the hull and the bed can be calculated as

$$l_x = X + h_2 \cos\zeta + a \sin\alpha \cos\eta (1 - \cos\Theta) - a \cos\alpha \sin\Theta$$

where $h_2 \equiv (h - a\cos\alpha)\tan\chi$ in terms of prescribed parameters,

$$l_y = h_2 \sin\zeta, \qquad \text{and} \qquad l_z = Z + h - a\cos\alpha\cos\Theta + a\sin\alpha\cos\eta\sin\Theta.$$

Further elementary geometry applied to the two mooring line segments provides the two relations

$$r_2(\hat{r}\sin\beta_1 + \cos\beta_2) = \sqrt{l_x^2 + l_y^2} \tag{A.4}$$

and

$$r_2(\hat{r}\cos\beta_1 + \sin\beta_2) = l_z \tag{A.5}$$

where β_1 is the angle the upper mooring line makes to the vertical at the hull and β_2 is the angle the lower mooring line makes with the horizontal at the bed. These two relations implicitly determine β_1 and β_2 in terms of (X, Θ, Z).

The tensions T_1 and T_2 in upper and lower lines follow from a quasi-static force balance (i.e. we assume no inertial effects from the moving lines in this model) to give

$$\begin{pmatrix} T_1 \\ T_2 \end{pmatrix} = \frac{m_l g}{\cos(\beta_1 + \beta_2)} \begin{pmatrix} \cos\beta_2 \\ \sin\beta_1 \end{pmatrix}. \tag{A.6}$$

Thus l_x, l_y, l_z and β_1, β_2, ζ are all functions of (X, Θ, Z) and hence so are T_1, T_2. To determine the static configuration, including static tensions, we substitute $(X, \Theta, Z) = (0, 0, 0)$, we fix the angle $\beta_1 = \lambda\chi$ where $\lambda < 1$ becomes the final mooring parameter.

Thus the static angle β_2 can be deduced from

$$\cos(\beta_2 + \chi) = \hat{r}\sin(\chi(1 - \lambda)). \tag{A.7}$$

which combine (A.4) and (A.5), and then

$$r_2 = (h - a\cos\alpha)/(\hat{r}\cos\lambda\chi + \sin\beta_2) \tag{A.8}$$

from which $r_1 = r_2\hat{r}$.

Meanwhile, a small amplitude assumption allows us to approximate the dynamic elements of the tension components T_{1x} as

$$\left(X(t)\frac{\partial T_{1x}}{\partial X} + \Theta(t)\frac{\partial T_{1x}}{\partial \Theta} + Z(t)\frac{\partial T_{1x}}{\partial Z} \right)_{(0,0,0)} \tag{A.9}$$

(similarly for T_{1z} and hence $M_{1\theta}$ from (A.2)).

Due to symmetry of the mooring configuration, the net effect of the four lines either reinforces additively or cancels out. For example, heave motions create dynamic tensions in each limb of the mooring line in all three components, but the net surge force and pitch moment induced by this heave motion is zero.

Thus, the dynamic components of the forces/moments experienced by the hull in directions of surge, pitch and heave provided by the mooring system due to small displacements of the hull are summarised by the matrix representation

$$\boldsymbol{X}_m = -\begin{pmatrix} K_{11} & K_{12} & 0 \\ K_{21} & K_{22} & 0 \\ 0 & 0 & K_{33} \end{pmatrix} \begin{pmatrix} X \\ \Theta \\ Z \end{pmatrix}. \tag{A.10}$$

where

$$K_{11} = 4\frac{\partial T_{1x}}{\partial X}, \qquad K_{12} = 4\frac{\partial T_{1x}}{\partial \Theta}, \qquad K_{21} = 4\frac{\partial M_{1\theta}}{\partial X}, \qquad K_{22} = 4\frac{\partial M_{1\theta}}{\partial \Theta}, \qquad K_{33} = 4\frac{\partial T_{1z}}{\partial Z}.$$

Taking partial derivatives of (A.4), (A.5) with respect to X, Z and Θ and evaluating at $(X, \Theta, Z) = (0, 0, 0)$ we find, after considerable algebra

$$\begin{aligned} \frac{\partial \beta_1}{\partial X} &= \frac{\cos\zeta\cos\beta_2}{r_1\cos(\beta_1+\beta_2)}, & \frac{\partial \beta_1}{\partial Z} &= \frac{\sin\beta_2}{r_1\cos(\beta_1+\beta_2)}, \\ \frac{\partial \beta_2}{\partial X} &= \frac{\cos\zeta\sin\beta_1}{r_2\cos(\beta_1+\beta_2)}, & \frac{\partial \beta_2}{\partial Z} &= \frac{\cos\beta_1}{r_2\cos(\beta_1+\beta_2)}. \end{aligned} \tag{A.11}$$

Additionally, we can deduce that

$$\frac{\partial \zeta}{\partial X} = -\frac{\sin\zeta}{h_2}, \qquad \text{and} \qquad \frac{\partial \zeta}{\partial Z} = 0 \tag{A.12}$$

whilst $\partial_\Theta = -a\cos\alpha\partial_X + a\cos\eta\sin\alpha\partial_Z$.

With (A.1) the relations above are enough to determine the elements of the matrix (A.10)

$$K_{11} = \frac{4m_l g\cos^2\zeta}{r_2\cos^3(\beta_1+\beta_2)}\left(\frac{\cos^3\beta_2}{\hat{r}} + \sin^3\beta_1\right) + \frac{4m_l g\sin^2\zeta\sin\beta_1\cos\beta_2}{h_2\cos(\beta_1+\beta_2)}, \tag{A.13}$$

$$K_{33} = \frac{4m_l g}{r_2\cos^3(\beta_1+\beta_2)}\left(\frac{\cos\beta_2\sin^2\beta_2}{\hat{r}} + \cos^2\beta_1\sin\beta_1\right), \tag{A.14}$$

with

$$K_{12} = K_{21} = a(\cos\eta\sin\alpha K_{13} - \cos\alpha K_{11}), \tag{A.15}$$

$$K_{22} = a^2(\cos^2\alpha K_{11} - \cos\eta\sin 2\alpha K_{13} + \cos^2\eta\sin^2\alpha K_{33}) \tag{A.16}$$

in terms of an intermediary variable

$$K_{13} = \frac{4m_l g\cos\zeta}{r_2\cos^3(\beta_1+\beta_2)}\left(\frac{\cos^2\beta_2\sin\beta_2}{\hat{r}} + \cos\beta_1\sin^2\beta_1\right). \tag{A.17}$$

In these definitions, dynamic variables are evaluated at their static values: in particular $\beta_1 = \lambda\chi$ in terms of given mooring parameters and β_2 and r_2 are given by (A.7) and (A.8). The symmetry of the matrix in (A.10) is expected. Simplifications made under special cases have been used to check the validity of the spring constants.

Appendix A.2. Elastic mooring system

Here a model of a taut mooring system with extensible limbs is considered, see Fig. A.11(b). This model is used only in the comparison with the experiments in Section 4. There are fewer model parameters than in the previous system. Each mooring limb comprises a single taut elastic mooring line of elastic stiffness λ and pre-stressed tension T_0 when extended to length L_0 in the static configuration. The line makes an angle χ with the vertical at the point of attachment as in the catenary example. Thus $L_0 = (h - a\cos\alpha)/\cos\chi)$ whilst the tension T_1 in the line attached to the hull is modelled by the Hookean relation

$$T_1 = T_0 + \lambda\left(\sqrt{l_x^2 + l_y^2 + l_z^2} - L_0\right).$$

A simpler application of the ideas given previously leads to

$$K_{11} = 4\lambda \sin^2\chi \cos^2\zeta + \frac{4T_0}{L_0}(1 - \sin^2\chi\cos^2\zeta), \tag{A.18}$$

$$K_{33} = 4\lambda \cos^2\chi + \frac{4T_0}{L_0}\sin^2\chi \tag{A.19}$$

and the intermediate variable

$$K_{13} = 4\left(\lambda - \frac{T_0}{L_0}\right)\sin\chi\cos\chi\cos\zeta \tag{A.20}$$

allows $K_{21} = K_{12}$ and K_{22} to follow from (A.15) and (A.16) as before.

Appendix B. Formulation of governing equations

In this Appendix, the equations of motion of the pendulum and the sphere are derived from the Euler-Lagrange equations. A hollow spherical shell of radius a, mass m_s, thickness d_s and density ρ_s has power take off machinery represented by a point mass, m_{pto}, positioned at the centre of the sphere and a point mass m_b representing ballast which is assumed to sit at the bottom of the sphere. The sum of these three fixed masses is denoted $M = m_s + m_{pto} + m_b$, its centre of mass located at $z = -L$ where $L = am_b/M$, and its moment of inertia about the origin is I where we calculate

$$I = a^2\left(m_b + \frac{2m_s}{5}\left(\frac{1-(a-d_s)^5/a^5}{1-(a-d_s)^3/a^3}\right)\right). \tag{B.1}$$

The sphere contains a compound pendulum which rotates through an angle $\theta(t)$ clockwise about the horizontal y-axis. The pendulum is assumed to be rotationally symmetric about the vertical central axis and has an annular central cross-section; it has a outer radius $c < a$, an inner radius $b < c$ and subtends to an angle of 2ξ, as shown in Fig. 2. The pendulum has a density ρ_p and has corresponding mass

$$m = \tfrac{2}{3}\rho_p(c^3 - b^3)(1 - \cos\xi)\pi. \tag{B.2}$$

The natural length l of the pendulum, being the distance from the origin to its centre of mass is calculated to be

$$l = \tfrac{3}{8}\frac{(c^4 - b^4)}{(c^3 - b^3)}(1 + \cos\xi). \tag{B.3}$$

The pendulum also has a moment of inertia about the origin which we denote by mk^2, where k is the radius of gyration of the pendulum defined by

$$k^2 = \tfrac{1}{10}\frac{(c^5 - b^5)}{(c^3 - b^3)}c^2(4 + \cos\xi(1 + \cos\xi)). \tag{B.4}$$

We note that, in the absence of damping, the resonant period of small amplitude pendulum motions are given by

$$T = \frac{2\pi}{\omega}, \qquad \text{with} \qquad \omega^2 = \frac{gl}{k^2}. \tag{B.5}$$

In motion, the centre of sphere is $(X(t), Z(t))$ and it rotates through an angle $\Theta(t)$ clockwise about the origin. The sphere is restrained by mooring lines characterised by linear spring constants

K_{ij} representing the force in the direction i due to motion in direction j, $i, j = 1, 2, 3$. These are given in Appendix A. Thus, the potential energy of the sphere/pendulum/mooring system is then given by,

$$\mathcal{V}(X, Z, \Theta, \theta) = \tfrac{1}{2}\left(K_{11}X^2 + K_{22}\Theta^2 + K_{33}Z^2 + 2K_{12}X\Theta\right) + \tfrac{1}{2}\rho g S Z^2 - MgL\cos\Theta - mgl\cos\theta, \tag{B.6}$$

where ρ is the density of the fluid and $S = \pi a^2$ is the equilibrium water plane area of the sphere.

The kinetic energy for the system is the sum of the kinetic energies for the sphere/ballast and that of the pendulum given by

$$\begin{aligned}\mathcal{T}(\dot{X}, \dot{Z}, \dot{\Theta}, \dot{\theta}, \Theta, \theta) = {} & \tfrac{1}{2}I\dot{\Theta}^2 + \tfrac{1}{2}mk^2\dot{\theta}^2 + \tfrac{1}{2}M(\dot{X}^2 + \dot{Z}^2 - 2L\dot{\Theta}(\dot{X}\cos\Theta - \dot{Z}\sin\Theta)) \\ & + \tfrac{1}{2}m\left(\dot{X}^2 + \dot{Z}^2 - 2l\dot{\theta}(\dot{X}\cos\theta - \dot{Z}\sin\theta)\right).\end{aligned} \tag{B.7}$$

A linear damping mechanism is connected to the pendulum, which acts in proportion to the rate of rotation of the pendulum with respect to the rotation of the sphere in pitch in order to extract power from the system. The linearised damping is included via the Rayleigh dissipation function [see 10], and we write

$$\mathcal{D}(\dot{\Theta}, \dot{\theta}) = \frac{1}{2}\gamma l^2(\dot{\theta} - \dot{\Theta})^2, \tag{B.8}$$

where γ represents a power take-off parameter.

The Euler-Lagrange equations are then given by

$$\frac{\partial}{\partial t}\frac{\partial \mathcal{L}}{\partial \dot{X}} - \frac{\partial \mathcal{L}}{\partial X} + \frac{\partial \mathcal{D}}{\partial \dot{X}} = F_{w,x}, \tag{B.9}$$

$$\frac{\partial}{\partial t}\frac{\partial \mathcal{L}}{\partial \dot{\Theta}} - \frac{\partial \mathcal{L}}{\partial \Theta} + \frac{\partial \mathcal{D}}{\partial \dot{\Theta}} = 0, \tag{B.10}$$

$$\frac{\partial}{\partial t}\frac{\partial \mathcal{L}}{\partial \dot{Z}} - \frac{\partial \mathcal{L}}{\partial Z} + \frac{\partial \mathcal{D}}{\partial \dot{Z}} = F_{w,z}, \tag{B.11}$$

$$\frac{\partial}{\partial t}\frac{\partial \mathcal{L}}{\partial \dot{\theta}} - \frac{\partial \mathcal{L}}{\partial \theta} + \frac{\partial \mathcal{D}}{\partial \dot{\theta}} = 0, \tag{B.12}$$

where $\mathcal{L} = \mathcal{T} - \mathcal{V}$ and $F_{w,x}(t)$ and $F_{w,z}(t)$ represent the external horizontal and vertical wave forces acting on the sphere. Applying equations (B.9)–(B.12) to (B.6)–(B.8) and linearising on the assumption of small amplitude motions gives

$$\begin{aligned}(M+m)\ddot{X} - ML\ddot{\Theta} - ml\ddot{\theta} &= F_{w,x} - K_{11}X - K_{12}\Theta \\ I\ddot{\Theta} - ML\ddot{X} &= -K_{22}\Theta - K_{12}X - MgL\Theta + \gamma l^2(\dot{\theta} - \dot{\Theta}), \\ (M+m)\ddot{Z} &= F_{w,z} - (K_{33} + \rho g S)Z \\ mk^2\ddot{\theta} - ml\ddot{X} &= -mlg\theta - \gamma l^2(\dot{\theta} - \dot{\Theta}).\end{aligned} \tag{B.13}$$

We shall assume incident waves of a single radian frequency ω and, since our governing equations are linear, a time harmonic dependence can be factorised from all dynamic variables and we write

$$\begin{aligned}[F_{w,x}, F_{w,z}] &= \mathrm{Re}\{(-\mathrm{i}gA/\omega)[X_{w,x}, X_{w,z}]\mathrm{e}^{-\mathrm{i}\omega t}\}, \\ [\dot{X}, \dot{Z}, l\dot{\Theta}, l(\dot{\theta} - \dot{\Theta})] &= \mathrm{Re}\{(-\mathrm{i}gA/\omega)[U, Z, \Omega, \Omega_r]\mathrm{e}^{-\mathrm{i}\omega t}\}\end{aligned} \tag{B.14}$$

where A is the incident wave amplitude so that $X_{w,x}$, $X_{w,z}$, U, V, Ω and Ω_r are all complex frequency dependent variables encoding amplitude and phase, respectively, of the surge and heave wave exciting forces, the surge and heave velocities, and scaled angular velocities of the sphere and the pendulum, relative to the sphere. The scaling of angular velocities by l assists with subsequent non-dimensionalisation and the introduction of relative velocity Ω_r as a proxy for the pendulum rotation is important in allowing the governing equations to be expressed in a natural symmetric manner as shown below. Thus, applying the decompositions (B.14) to (B.13) results in

$$\begin{aligned}
-\mathrm{i}\omega(M+m)U + \mathrm{i}\omega M\hat{L}\Omega + \mathrm{i}\omega m(\Omega+\Omega_r) &= X_{w,x} - \frac{\mathrm{i}}{\omega}K_{11}U - \frac{\mathrm{i}}{\omega l}K_{12}\Omega,\\
-\mathrm{i}\omega\hat{I}\Omega + \mathrm{i}\omega M\hat{L}U &= -\frac{\mathrm{i}}{\omega l}K_{12}U - \frac{\mathrm{i}}{\omega}(K_{22}/l^2 + (Mg/l)\hat{L})\Omega + \gamma\Omega_r,\\
-\mathrm{i}\omega(M+m)V &= X_{w,z} - \frac{\mathrm{i}}{\omega}\left(K_{33}+\rho g S\right)V,\\
-\mathrm{i}\omega m\hat{k}^2(\Omega+\Omega_r) + \mathrm{i}\omega mU &= -\frac{\mathrm{i}}{\omega}(mg/l)(\Omega+\Omega_r) - \gamma\Omega_r
\end{aligned} \tag{B.15}$$

where $\hat{L} = L/l$, $\hat{I} = I/l^2$ and $\hat{k} = k/l$. It is clear from the third line of (B.15) that the heave motions are independent, or uncoupled, to surge, pitch and pendulum motions.

The result of adding the fourth to the second equation is

$$\begin{aligned}
-\mathrm{i}\omega(\hat{I}+m\hat{k}^2)\Omega - \mathrm{i}m\hat{k}^2\Omega_r + \mathrm{i}\omega(M\hat{L}+m)U &= -\frac{\mathrm{i}}{\omega l}K_{12}U\\
&\quad - \frac{\mathrm{i}}{\omega}\big(K_{22}/l^2 + (Mg/l)\hat{L} + (mg/l)\big)\Omega - \frac{\mathrm{i}}{\omega}(mg/l)\Omega_r.
\end{aligned} \tag{B.16}$$

Organising the first line of (B.15), (B.16) and then the last line of (B.15) as a 3×3 matrix equation gives

$$-\mathrm{i}\omega\mathsf{M}\boldsymbol{U} = \boldsymbol{X}_w - \frac{\mathrm{i}}{\omega}\left(\mathsf{C}+\mathsf{K}\right)\boldsymbol{U} - \gamma\mathsf{G}\boldsymbol{U} \tag{B.17}$$

where the vectors are

$$\boldsymbol{U} = (U,\Omega,\Omega_r)^T \qquad \text{and} \qquad \boldsymbol{X}_w = (X_{w,x},0,0)^T, \tag{B.18}$$

and the matrices are

$$\mathsf{M} = \begin{pmatrix} M+m & -M\hat{L}-m & -m\\ -M\hat{L}-m & \hat{I}+m\hat{k}^2 & m\hat{k}^2\\ -m & m\hat{k}^2 & m\hat{k}^2 \end{pmatrix}, \qquad \mathsf{C} = \begin{pmatrix} 0 & 0 & 0\\ 0 & (Mg/l)\hat{L}+mg/l & mg/l\\ 0 & mg/l & mg/l \end{pmatrix}, \tag{B.19}$$

and

$$\mathsf{K} = \begin{pmatrix} K_{11} & K_{12}/l & 0\\ K_{12}/l & K_{22}/l^2 & 0\\ 0 & 0 & 0 \end{pmatrix}, \quad \mathsf{G} = \begin{pmatrix} 0 & 0 & 0\\ 0 & 0 & 0\\ 0 & 0 & 1 \end{pmatrix}. \tag{B.20}$$

The system defined by (B.17) is similar to that described in [5] for the SEAREV device.

It should be noted that we have not included the dynamic effects of the catenary mooring lines on the equations of motion of the coupled sphere/pendulum system. For heave and pitch motions there will be no net restoring forces from the mooring line mass but there will be extra inertia

contributions. In reality, the mooring lines would also exhibit added inertia due to acceleration of the fluid and viscous damping losses due to its motion. These terms have been neglected in the model above for simplicity and on the assumption they will have a small effect on the overall dynamics.

Appendix C. Wave climate parametrisation

This appendix describes the process used in order to be able to predict the device performance over a given wave energy spectrum for a particular wave energy test site. [14] provide scatter diagrams of sea states for a number of wave energy test sites, including EMEC illustrated in Fig. C.12, which we will use in this study. Data is binned in intervals of 1 s for T_z, the zero-crossing period, and 0.5 m for H_s, and the occurrence of each sea state over a given period is provided. Using this data we define a function $P(H_s, T_p)$ to be the joint probability of the occurrence of a pair of parameter values; it is assumed that $T_p = \sqrt{2}T_z$.

We employ the two parameter spectrum developed by [3],

$$S(T) = \frac{5}{16} H_s^2 \frac{T^5}{T_p^4} \mathrm{e}^{-\frac{5}{4}(T/T_p)^4}, \tag{C.1}$$

where H_s denotes the significant wave height – defined as the mean height of the highest third of waves – and T_p the peak wave period in the spectrum. Then, using the probability function $P(H_s, T_p)$, define a modified spectrum,

$$\tilde{S}(T) = \sum_{H_s} \sum_{T_p} P(H_s, T_p) S(T; H_s, T_p), \tag{C.2}$$

where the sums extend over the full range of expected sea states. Thus $\tilde{S}(T)$ takes into account the probability of occurrence of each sea state.

We also incorporate a function to describe the spread of the energy density of the incident wave field, such that the incoming waves are no longer assumed to be unidirectional.

The directional spread of the incident waves is incorporated using a normalised cosine($2s$) function,

$$G(\theta) = \begin{cases} F(s) \cos^{2s}(\theta) & |\theta| < \pi/2, \\ 0 \qquad \text{otherwise}, \end{cases} \qquad \text{where} \quad F(s) = \frac{2^{2s-1}}{\pi} \frac{\Gamma^2(s+1)}{\Gamma(2s+1)}, \tag{C.3}$$

where θ is the angle of incidence of the incoming wave. We have taken the predominant wave direction to be zero. The variable s is known as the spread parameter that can be taken to be constant or frequency dependent. We set $s = 12$, which is commonly used as an estimate for practical purposes, [17]. The function $G(\theta)$ is normalised such that,

$$\int_{-\pi}^{\pi} G(\theta) \mathrm{d}\theta = 1. \tag{C.4}$$

The mean incident wave power per unit crest length is then given by

$$\overline{W}_{inc} = \rho g \int_{-\pi}^{\pi} \int_{0}^{\infty} c_g(T) \tilde{S}(T) G(\theta) T^{-2} \, \mathrm{d}T \, \mathrm{d}\theta, \tag{C.5}$$

in units of kW/m, where $c_g(T)$ is the group velocity of the waves as a function of period [see 8, for example] which, in deep water is equivalent to $c_g = g/(2\omega)$, and $\tilde{S}(T)$ the modified wave energy density spectrum, given in (C.2).

Tz/Hs	3.5	4.5	5.5	6.5	7.5	8.5	9.5	10.5	11.5	12.5	13.5	14.5
0.25	2.698	3.680	1.976	0.805	0.362	0.254	0.139	0.032	0.002			
0.75	2.312	9.523	5.893	2.098	0.747	0.185	0.086	0.041	0.002			
1.25	0.461	6.595	7.096	2.996	1.150	0.334	0.108	0.039		0.009	0.007	0.002
1.75	0.132	2.070	7.783	2.871	1.047	0.358	0.141	0.021			0.005	
2.25		0.293	5.497	3.904	1.099	0.324	0.187	0.067	0.009			
2.75		0.026	1.154	5.159	1.154	0.238	0.139	0.053	0.017	0.002		0.002
3.25		0.005	0.139	3.334	2.036	0.254	0.108	0.036	0.019	0.007		
3.75			0.014	0.725	2.760	0.422	0.094	0.014	0.009	0.002		
4.25				0.058	1.755	0.559	0.096	0.041	0.019		0.005	0.005
4.75				0.007	0.437	0.876	0.120	0.026	0.014	0.005		
5.25					0.046	0.780	0.146	0.032	0.005			
5.75						0.272	0.259	0.007	0.002	0.005		
6.25				0.002	0.005	0.055	0.231	0.014	0.005			
6.75					0.005	0.005	0.144	0.081	0.005			
7.25							0.067	0.113		0.002		
7.75							0.032	0.111	0.002	0.002		
8.25							0.007	0.032	0.021			
8.75								0.026	0.026			
9.25								0.002	0.019	0.005		
9.75									0.014	0.002		
10.25									0.007	0.002		
10.75										0.002		
11.25										0.005		

Figure C.12: A scatter plot of the probabilities of expected sea states at the EMEC wave site, data from [14].

Acknowledgments

The authors would like to acknowledge funding from EPSRC grant numbers EP/N508640/1 and EP/N508652/1. The authors are also grateful to WITT Limited and other project partners of the INNOVATE UK consortium for direction and support on this project.

References

[1] Babarit, A., 2015. A database of capture width ratio of wave energy converters. Renewable Energy 80, 610–628.

[2] Babarit, A., Hals, J., Muliawan, M., Kurniawan, A., Moan, T., Krokstad, J., 2012. Numerical benchmarking study of a selection of wave energy converters. Renewable Energy 41, 44–63.

[3] Bretschnieder, C., 1959. Wave variability and wave spectra for wind-generated gravity waves. Tech. rep., U.S. Army, Corps of Engineers.

[4] Clément, A., Babarit, A., Gilloteaux, J.-C., Josset, C., Duclos, G., 2005. The SEAREV wave energy converter. In: Proceedings of the 6th Wave and Tidal Energy Conference, Glasgow, UK.

[5] Cordonnier, J., Gorintin, F., De Cagny, A., Clément, A., Babarit, A., 2015. SEAREV: Case study of the development of a wave energy converter. Renewable Energy 80, 40–52.

[6] Crowley, S., Porter, R., Evans, D., 2013. A submerged cylinder wave energy converter. Journal of Fluid Mechanics 716, 566–596.

[7] Evans, D., 1981. Maximum wave-power absorption under motion constraints. Applied Ocean Research 3 (4), 200–203.

[8] Evans, D., 1981. Power from water waves. Annual Review of Fluid Mechanics 13 (1), 157–187.

[9] Evans, D., Porter, R., 2012. Wave energy extraction by coupled resonant absorbers. Phil. Trans. of the Royal Soc. of London A 370 (1959), 315–344.

[10] Goldstein, H., 1974. Classical mechanics. Addison-Wesley Pub. Co.

[11] Hulme, A., 1982. The wave forces acting on a floating hemisphere undergoing forced periodic oscillations. Journal of Fluid Mechanics 121, 443–463.

[12] Ibrahim, R. A., 2005. Liquid sloshing dynamics: theory and applications. Cambridge University Press.

[13] Newman, J., 1976. The interaction of stationary vessels with regular waves. In: 11th Symp. on Naval Hydrodynamics.

[14] Nielsen, K., Pontes, T., 2010. Generic and site-related wave energy data. Report T02-1.1 OES IA Annex II Task.

[15] Pizer, D., 1993. Maximum wave-power absorption of point absorbers under motion constraints. Applied Ocean Research 15 (4), 227–234.

[16] Srokosz, M., 1979. The submerged sphere as an absorber of wave power. Journal of Fluid Mechanics 95 (04), 717–741.

[17] Tucker, M., 1991. Waves in Ocean Engineering: Measurement, analysis, interpretation. Ellis Horwood.

[18] Wello Oy, 2014. The Wello Penguin at EMEC. `http://www.wello.eu/en/penguin.php`